Wavelet-Based Discriminant Feature Analysis of Marine Plastic Litter Spectra and Matching via Magnitude Gradient Cosine Similarity

José Maravalhas-Silva
INESC TEC
Porto, Portugal
0000-0002-5503-2486

Nuno A. Cruz
Senior Member, IEEE
INESC TEC, FEUP-DEEC
Porto, Portugal
0000-0001-6365-9492

***Abstract*—In hyperspectral remote sensing, it is common to perform direct analysis of reflectance signals to identify key absorption features, and to apply techniques like the Spectral Angle Mapper to compare spectra and generate a similarity score.**

In this paper, we introduce the first application of the Continuous Wavelet Transform (CWT) in the context of hyperspectral remote sensing of marine plastic litter. First, we use the CWT to decompose plastic litter reflectance spectra from publicly available datasets and analyze its structure from the perspective of its frequency content at different wavelengths. Then, we propose a matching technique based on the cosine similarity of the magnitude gradients of the CWTs, named CWT Gradient Matching (CWTGM).

Our results show that the CWT can be used to identify features which may otherwise prove difficult to analyze, and may also be useful in guiding sensor design. We also demonstrate that the CWTGM technique may be a viable option to measure similarity based on the frequency content of spectral reflectance signals.

***Index Terms*—Remote Sensing, Hyperspectral, Marine Litter, Signal Processing, Continuous Wavelet Transform**

I. Introduction

Marine plastic pollution remains a persistent global challenge [1, 2]. While researchers are now fairly certain on the orders of magnitude of plastic waste that makes its way to aquatic environments, exact numbers remain unclear. A 2022 report by the Organisation for Economic Co-operation and Development (OECD) indicates that an estimated $6\,\mathrm{Mt}$ of plastic debris reach aquatic environments, with an uncertainty range spanning from $4\,\mathrm{Mt}$ to $9\,\mathrm{Mt}$ [1].

Part of the reason for the existence of such uncertainties is insufficient data [3]. Remote sensing technologies have been a promising tool to address this, as they offer the ability to cover large and logistically challenging areas with little to no interference with the marine ecosystem, and the use of both airborne and spaceborne platforms can be combined to fill each other's gaps [4, 5].

This work is funded with national funds through FCT – Fundação para a Ciência e a Tecnologia, I.P., within the scope of the studentship for Doctoral Research Funding Programme, grant number SFRH/BD/151463/2021, and with national funds through FCT – Fundação para a Ciência e a Tecnologia, I.P., under the support UID/50014/2023 (https://doi.org/10.54499/UID/50014/2023).

In existing literature, most analysis of marine plastic litter spectra are based on identifying wavelength regions of strong absorption, and how these relate to material type [6–10].

To enable the comparison between spectra, authors often treat spectra as vectors in $\mathbb{R}^B$, where B represents the number of sampled spectral bands, and compute their cosine similarities [6, 7, 11]. In this context, the angle derived from the cosine similarity is often referred to as the Spectral Angle Mapper (SAM), and is commonly used to compare spectra.

Let $s_1[\lambda]$ and $s_2[\lambda]$ denote two discrete functions corresponding to sampled spectra, where $\lambda \in \{\lambda_1, \ldots, \lambda_B\}$ is a discrete variable representing the set of sampled wavelengths. The spectra are then treated as vectors $\boldsymbol{s_1}, \boldsymbol{s_2} \in \mathbb{R}^B$ such that:

$$\boldsymbol{s_1} = [s_1[\lambda_1], s_1[\lambda_2], \ldots, s_1[\lambda_B]]^T \tag{1a}$$

$$\boldsymbol{s_2} = [s_2[\lambda_1], s_2[\lambda_2], \ldots, s_2[\lambda_B]]^T \tag{1b}$$

The SAM similarity score, which is simply the angle $\theta_{s_2}^{s_1}$ between vectors $\boldsymbol{s_1}$ and $\boldsymbol{s_2}$, is given as:

$$SAM(\boldsymbol{s_1}, \boldsymbol{s_2}) = \theta_{s_2}^{s_1} = \arccos\left(\frac{\boldsymbol{s_1} \cdot \boldsymbol{s_2}}{\|\boldsymbol{s_1}\| \, \|\boldsymbol{s_2}\|}\right) \tag{2a}$$

$$= \arccos\left(\frac{\sum_{i=1}^{B} s_1[\lambda_i] s_2[\lambda_i]}{\sqrt{\sum_{i=1}^{B} s_1[\lambda_i]^2 \sum_{i=1}^{B} s_2[\lambda_i]^2}}\right) \tag{2b}$$

The authors of [7] were among the first to have sampled the reflectance spectra of ocean-bound plastics. In it, they make use of SAM to compare spectra. While they observed the consistency of certain absorption features in the short-wave infrared (SWIR) region across different samples, they also emphasized that polymer blending and weathering effects complicate the spectral matching process, with later works appearing to support this claim [8]. A later review summarizes spectral features identified by multiple studies [6].

In our review of the literature, we noticed that current approaches tend to treat reflectance spectra as a set of isolated features - drops or peaks at specific wavelengths - rather than a continuous signal with underlying structural patterns. While some methods may implicitly account for broader

characteristics of the signal, to the best of our knowledge, there have been no prior studies that explicitly analyze spectral signatures from a frequency content perspective.

In this work, we aim to address this gap by presenting what we believe to be the first application of the non-stationary signal analysis technique known as the Continuous Wavelet Transform (CWT) to the domain of hyperspectral remote sensing of marine plastic litter. The CWT enables the decomposition of signals into components at multiple spatial frequencies for a given wavelength [12], thus facilitating the analysis of said signal's structure. This allows us to analyze discriminant features, assess the spectral resolution required to capture these features, and - by processing the CWT - even compute similarity scores between different spectra.

II. Dataset Description and Preprocessing

We make use of two publicly available datasets: one by Knaeps et al [13] and another by Leone et al [14], which we have denoted datasets (K) and (L), respectively. Note that for (L), we made use of the updated version.

Both datasets make use of an ASD FieldSpec 4 spectroradiometer, which records data from $350\,\mathrm{nm}$ to $2500\,\mathrm{nm}$. Since the instrument actually comprises multiple sensors, the spectral resolution is not consistent across the entire range, but is never lower than $10\,\mathrm{nm}$. Besides an upsampling to a resolution of $1\,\mathrm{nm}$, the datasets contain no further processing.

The use of different sensors also result in splicing artifacts at the near $1000\,\mathrm{nm}$ and $1800\,\mathrm{nm}$, which the authors of (K) and (L) recommend correcting for [13, 14].

A. Splice Correction

Splice correction for (K) followed the authors' recommendation [13]: the difference between $1000\,\mathrm{nm}$ and $1001\,\mathrm{nm}$ was used to adjust reflectance values below $1000\,\mathrm{nm}$, and the difference between $1800\,\mathrm{nm}$ and $1801\,\mathrm{nm}$ for values above $1800\,\mathrm{nm}$.

For the (L) dataset, we observed that splicing near $1800\,\mathrm{nm}$ was inconsistent, occurring either at $1800\,\mathrm{nm}$ or $1830\,\mathrm{nm}$. For this reason, our implementation of splicing correction for (L) is the same as (K) for $1000\,\mathrm{nm}$, but differs for the $1800\,\mathrm{nm}$ region. It compares the difference between $1800\,\mathrm{nm}$ and $1801\,\mathrm{nm}$ and between $1830\,\mathrm{nm}$ and $1831\,\mathrm{nm}$, and applies correction based on the larger of the two.

B. Sample Selection

From the available data, we chose to analyze spectra of dry plastic samples with unambiguous composition.

While (L) contains Fourier-transform infrared spectroscopy (FTIR) confirmation for some of its spectra, (K) does not, which complicates the selection process. For this reason, from (K) we only selected a single polypropylene (PP) spectrum, and excluded all other samples for the following reasons:

- Transparent materials were excluded due to the potential presence of spectral features that are not idiosyncratic to the molecular structure of the polymer type, but rather arise from measurement-related optical effects. While these effects could be characterized, the lack of control over how the spectra were sampled (e.g., viewing angle, sample geometry) makes such analysis infeasible.
- In two studies analyzing the presence of microplastics in food containers and plastic cups, FTIR is used to confirm the composition of the items under study. Both studies indicate that plastic polyethylene (PE) cups are usually made of wood pulp paper with a film of PE sprayed on top [15, 16]. If such film is not perfectly opaque, then it follows that spectral contamination from the underlying material will occur. Furthermore, the images of PP cups in [15] appear to match those of the low-density PE (LDPE) cups from [13], but also appear to match the images of PE cups from [16]. This indicates that visual inspection alone may not be sufficient to determine the composition of the cups from [13], and even if these were adequately marked as being made from LDPE, we do not know if the manufacturing process is the same as mentioned in [15] and in [16]. Therefore, out of fear of incorrect labeling and spectral contamination, we have decided against the inclusion of the LDPE cups from [13] in our analysis.
- We excluded the polyester rope in [13] since polyester is not a specific polymer, but rather a family of different polymers.
- We excluded all samples of unspecified polymer type.

This left us with very few spectra, but we still opted to include one PP sample from (K) in an attempt to reduce potential biases from relying solely on spectra from (L).

From (L), we selected PP, PE, and polystyrene (PS) samples, all containing FTIR confirmation of polymer type. The (L) dataset provides more than 5000 spectra, containing multiple consecutive replicates - which the authors designated "pseudo-replicas" - and replicates performed in different days [14]. While the authors recommend averaging multiple pseudo-replicas, we chose not to. Our reasoning is that hyperspectral sensors on airborne or spaceborne platforms will likely never achieve the signal-to-noise ratio (SNR) of scientific spectroradiometers. Thus, any SNR improvement and subsequent features revealed by such processing would be unattainable outside the lab.

In total, we have selected 9 spectra of three different polymer types: PP, PE and PS. Table I contains a list of the selected spectra with the naming scheme used for this work, as well as the original names in their respective datasets.

TABLE I
List of Samples Under Analysis

ID	Original Sample Name	Polymer	Dataset
PP_1	Blue_PP_rope_roll_d	PP	(K)
PP_2	PP_d_NA_NA_Carat_pristine	PP	(L)
PP_3	PP_d_NA_NA_Toc_pristine	PP	(L)
PE_1	PE_d_NA_NA_Carat_pristine	PE	(L)
PE_2	BlueFoam_d_NA_NA_PoA_field	PE	(L)
PE_3	MilkBottle_d_NA_NA_PoA_field	PE	(L)
PS_1	PS_d_NA_NA_Carat_pristine	PS	(L)
PS_2	PS_d_NA_NA_VITO_pristine	PS	(L)
PS_3	PS_d_NA_NA_shop_pristine	PS	(L)

III. CWT Feature Analysis

A. Introduction to the CWT and Mother Wavelet Selection

The CWT of a signal, here adapted to be a continuous signal $s(\lambda)$ as a function of wavelength λ instead of time t, is defined by [12]:

$$\mathcal{W}_{s(\lambda)}(u,k) = \frac{1}{\sqrt{|k|}} \int_{-\infty}^{+\infty} s(\lambda)\psi^* \left(\frac{\lambda - u}{k}\right) d\lambda, \quad u,k \in \mathbb{R} \tag{3}$$

Where $\psi(\lambda)$, u, and k respectively represent the mother wavelet, its translation, and scaling factors.

The mother wavelet $\psi(\lambda)$ is a complex-valued function which is translated and scaled to analyze different sections of the original signal. The factor u centers the wavelet at different wavelengths, whereas the factor k adjusts the frequency of the wavelet. The latter effectively selects the resolution of the features under analysis: larger values of k stretch the wavelet, making it sensitive to low-frequency features spanning broad regions of the signal, while smaller values compress it, making it sensitive to high-frequency, highly localized features.

When making use of the CWT, one must first choose an appropriate mother wavelet, for which we chose Morse wavelets for their flexibility in the choice of two parameters, the time-domain decay B and frequency-domain decay γ, which optionally allow for additional control of the wavelet's overall shape [17, 18]. The possible range of u values is determined by signal length, such that the wavelets are translated to each sample of the signal. For k, one must choose the desired frequency resolution: by convention, the frequency axis is divided into octaves and sampled logarithmically, with a specified number of sampled frequency per octave, usually referred to as "voices".

In this work, we make use of MATLAB's implementation of the CWT, which uses Morse wavelets by default, with default values of time-bandwidth product $P^2 = B\gamma = 60$ and $\gamma = 3$ [17, 18]. We modified the number of voices per octave to the maximum allowed of 48. This was done to compensate for the fact that the reflectance signals from (K) and (L) are upsampled from $10\,\mathrm{nm}$ to $1\,\mathrm{nm}$, as retaining the default value of 10 would result in low frequency resolution for the spatial frequencies of interest.

B. Data Plots

To plot the CWT results, we compute its magnitude $\left|\mathcal{W}_{s(\lambda)}(u,k)\right|$, also known as a scalogram [12]. As wavelets are scaled and translated, those located near the edges of the data will extend over its boundaries. To address this, the data is extended, leading to edge effects. The cone of influence (COI) is the region where these effects become significant, and is marked on the scalograms with a dashed white line.

Although plastics can be manufactured in virtually any visible color, we still opted to include the entire spectral range to reduce edge effects. As a result, the COI appears asymmetrical in our plots, as we display only the results for wavelengths above $700\,\mathrm{nm}$ - approximately corresponding to the transition point from visible to near-infrared light.

C. Feature Analysis

We start by analyzing the scalograms for PP. Fig. 1 shows three PP spectra along with their respective scalograms. In the spectra, we can visually observe a strong absorption feature at $1700\,\mathrm{nm}$, as well as two other moderate features at $1200\,\mathrm{nm}$ and $1400\,\mathrm{nm}$. By looking at the scalograms, it is clear that these three features are also present, but we can now infer more about the underlying signal structure. For instance, the feature at $1700\,\mathrm{nm}$ appears as a medium-intensity triangular-shaped high-frequency region in the scalogram (highlighted with a red triangle in the figure), whereas the other two prominent features manifest as lower energy V-shaped high-frequency content (highlighted with a red square in the figure).

In Fig. 1, we can see that the spectrum of PP_3 presents less pronounced absorption features at $1200\,\mathrm{nm}$ and $1400\,\mathrm{nm}$, yet the scalogram presents the same overall shape as in the other two scalograms, albeit fainter.

When comparing PP to PE, the latter shown in Fig. 2, we can see that the previous three main features are also present on the spectra. However, looking at the scalograms, their structure is noticeably different. Instead of the triangular shape in the $1700\,\mathrm{nm}$ region, the PE scalograms present a triangular shape with a distinct curvature. For the other two features, we observe that, between $0.01\,\mathrm{nm}^{-1}$ and $0.05\,\mathrm{nm}^{-1}$, the feature at $1400\,\mathrm{nm}$ appears to form a narrow line on the scalogram, while the $1200\,\mathrm{nm}$ feature takes a wider, more triangular shape. The feature at $1400\,\mathrm{nm}$ also appears to have slightly lower overall intensity than the one at $1200\,\mathrm{nm}$. These nuanced differences are not present in the PP scalograms.

When comparing PP to PE and trying to distinguish between the two, the distinct curvature present on the PE scalograms at $1700\,\mathrm{nm}$ could be used to differentiate between the two materials. This could then be aided by the previously mentioned imbalances in frequency content between the $1200\,\mathrm{nm}$ and $1400\,\mathrm{nm}$ regions present in PE.

Finally, for PS, shown in Fig. 3, it is again easy to identify the main features directly from the spectrum. These are at $1150\,\mathrm{nm}$, $1700\,\mathrm{nm}$ and $2150\,\mathrm{nm}$. The most prominent one is again at $1700\,\mathrm{nm}$, however, looking at the scalogram, one can see that this feature has a different structure when compared to that of PP and PE. It also appears to be less consistent overall.

Another observation is that multiple regions where the scalograms consistently lack frequency components between samples of the same material, effectively appearing as "holes" in the scalograms. These could also serve as discerning features between materials.

We also find that the most consistent spatial frequency region across samples - and the one that allows for a clear distinction between PP, PE and PS samples - lies above $0.01\,\mathrm{nm}^{-1}$. This implies that, when designing a hyperspectral sensor with the goal of distinguishing between these polymers, a resolution finer than $50\,\mathrm{nm}$ is required, as coarser resolutions do not satisfy the Nyquist criterion for $0.01\,\mathrm{nm}^{-1}$. Based on the observed frequency content, we recommend a sampling resolution no coarser than $10\,\mathrm{nm}$, thus satisfying the Nyquist criterion up to $0.05\,\mathrm{nm}^{-1}$.

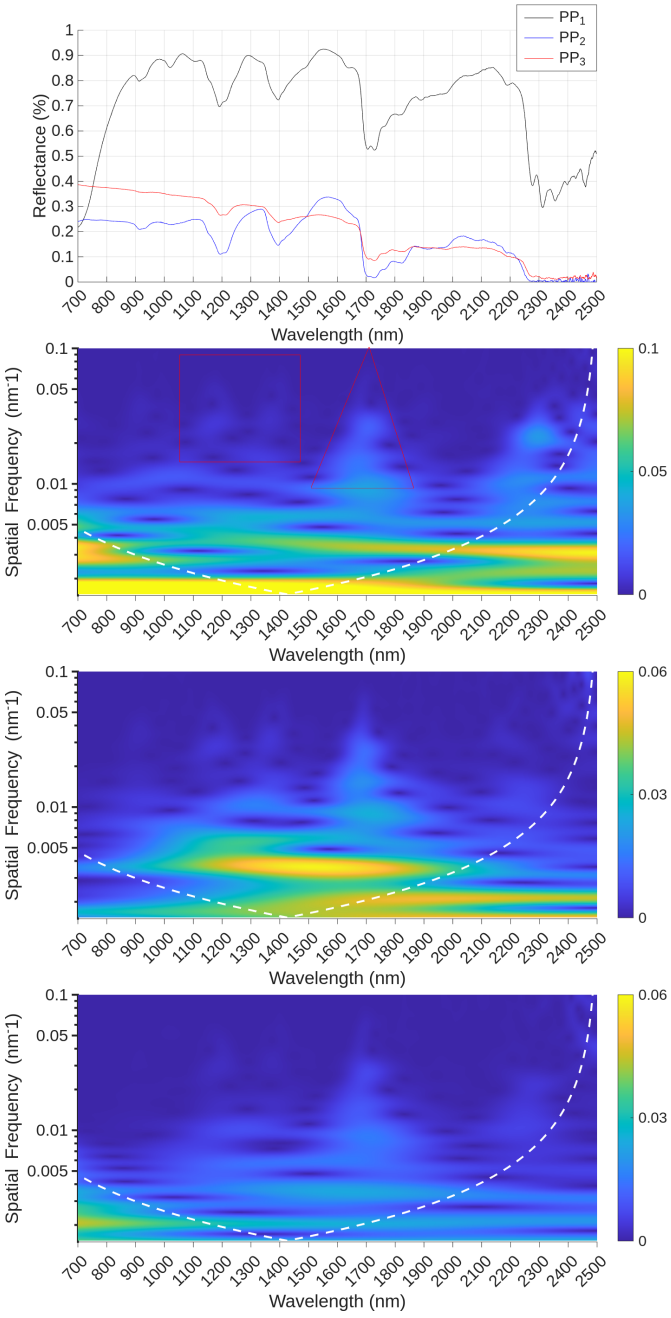

Fig. 1. Spectra and scalograms of PP Samples PP_1, PP_2 and PP_3. Respective scalograms from top to bottom. Prominent features observed in the spectrum are highlighted in red in the first scalogram (PP_1).

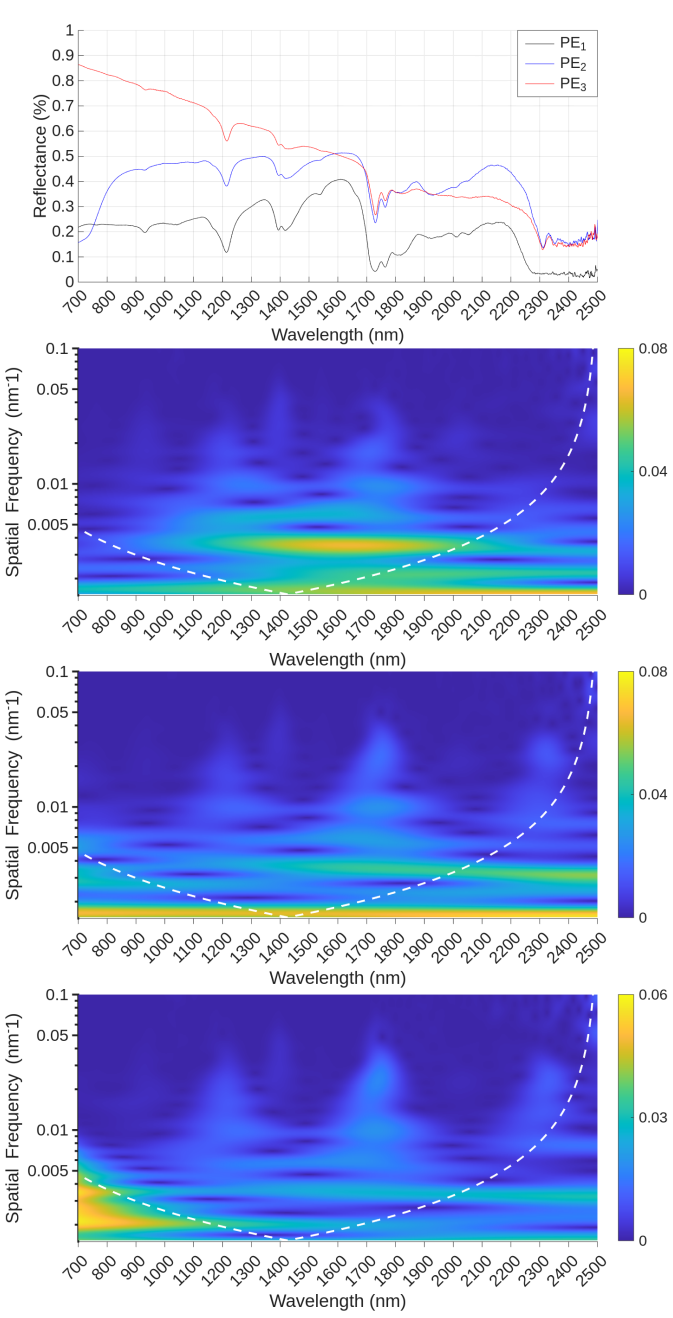

Fig. 2. Spectra and scalograms of PE Samples PE_1, PE_2 and PE_3. Respective scalograms from top to bottom.

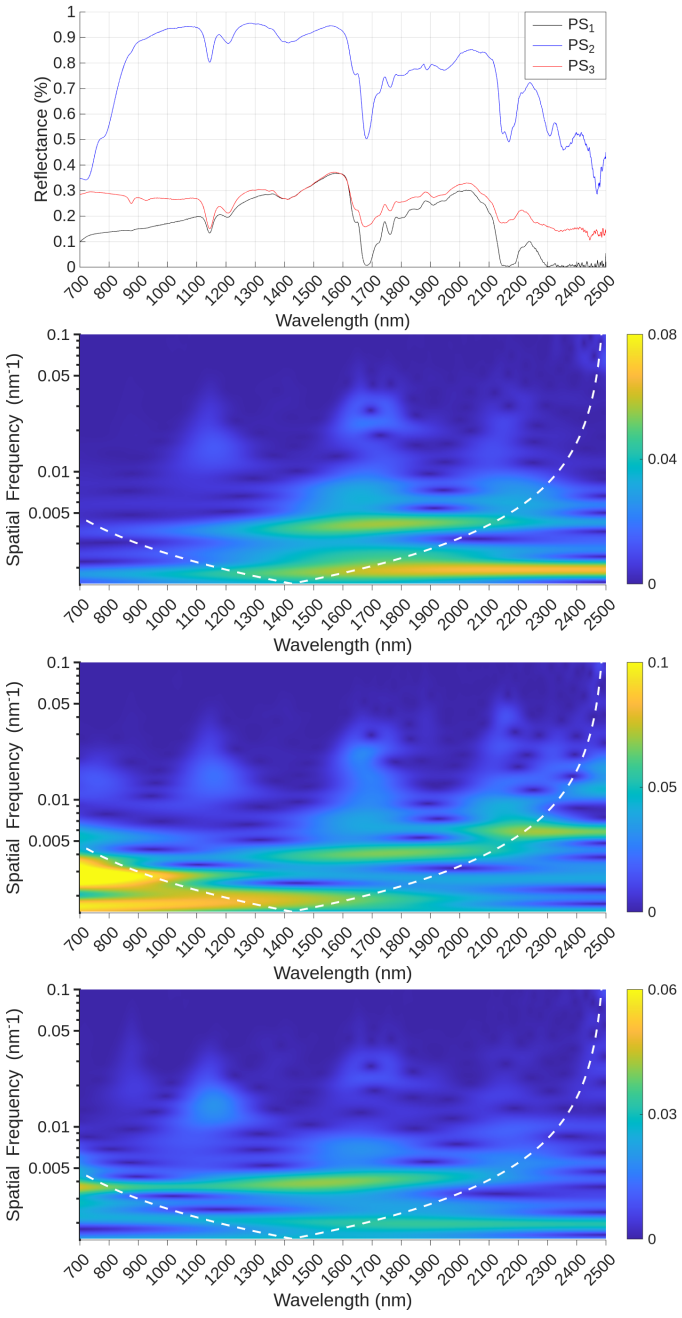

Fig. 3. Spectra and scalograms of PS Samples PS_1, PS_2 and PS_3. Respective scalograms from top to bottom.

IV. CWT Gradient Matching

While the visual analysis of CWT scalograms can provide an intuitive understanding of the data, it lacks quantitative rigor. Since our goal is to measure the similarity of the overall shape of the scalogram, we focus on local amplitude variations as opposed to global variations across the entire scalogram, and therefore rely on the cosine similarity of the gradients of the scalograms. We refer to this as the CWT Gradient Matching (CWTGM) algorithm.

Let $\mathcal{S}(u,k)$ be the scalogram of $\mathcal{W}(u,k)$ such that $\mathcal{S}(u,k) = |\mathcal{W}(u,k)|$. Then, let $G_x(u,k)$ and $G_y(u,k)$ be given by:

$$[G_x(u,k),\ G_y(u,k)] = \nabla \mathcal{S}(u,k) \tag{4}$$

Although scalograms are inherently two-dimensional, we include only $G_x(u,k)$ in the cosine similarity calculation. The motivation for this choice is two-fold. First, from a mathematical understanding of the CWT as shown in Eq. 3, we can see that each value of k selects a differently scaled wavelet which is then correlated with the original signal. This is equivalent to applying a bank of filters to the signal [12], and thus, variation along u reflects how the signal responds to filtering at scale k. In other words, $G_x(u,k)$ reveals how the signal reacts to the filters, and is therefore an intuitive way to capture the signal's structure as revealed through scale-specific filtering. The second reason is empirical: we observed that $G_x(u,k)$ captures most of the meaningful variations in the scalogram, while $G_y(u,k)$ remains smooth and its inclusion resulted in degraded performance. For these reasons, $G_y(u,k)$ is discarded to improve matching performance and computational efficiency.

Let $G_x^{s1}(u,k)$ and $G_x^{s2}(u,k)$ denote the horizontal gradients of the scalograms of signals $s_1(\lambda)$ and $s_2(\lambda)$. The CWTGM score $CWTGM_{s1}^{s2}$ can be calculated as follows:

$$CWTGM_{s1}^{s2} = \frac{G_x^{s1}(u,k) \cdot G_x^{s2}(u,k)}{||G_x^{s1}(u,k)||\ ||G_x^{s2}(u,k)||} \tag{5}$$

Fig. 4 shows the CWTGM scores for all plastic samples under analysis. The scores were computed only using wavelengths above $700\,\mathrm{nm}$. Based on our previous analysis of the scalograms, we chose to include the spatial frequencies between $0.01\,\mathrm{nm}^{-1}$ and $0.1\,\mathrm{nm}^{-1}$.

In an ideal scenario, the scores in Fig. 4 for in-group matches (e.g. PP_1 with PP_2 and PP_3) would be maximum (equal to 1.0), whereas the scores for out-group matches (e.g. any PP with any PE or PS) would be minimum (equal to 0). Therefore, one would expect to see three 3-by-3 blocks of perfect matches: one in the top left, another in middle, and a final one at bottom right of Fig. 4. In reality, the results are 1.0 only when the spectra are matched with themselves. Nonetheless, we can observe that CWTGM successfully matched each spectrum to those of the same polymer type, as the highest similarity score always occurs between spectra of the same material. The highest out-group match score is between PP_3 and PE_3, with a value of 0.41, whereas the lowest in-group score is between PS_3 and PS_2, with a value of 0.44. A threshold between these two values could therefore be used to correctly categorize each spectra by polymer type.

Given the out-group scores, PS is clearly the more distinguishable among the three polymer types. Meanwhile, the similarity scores between PP and PE spectra are closer than would be desirable, likely due to their main spectral features occurring at similar wavelengths, which introduces ambiguity in distinguishing between the two.

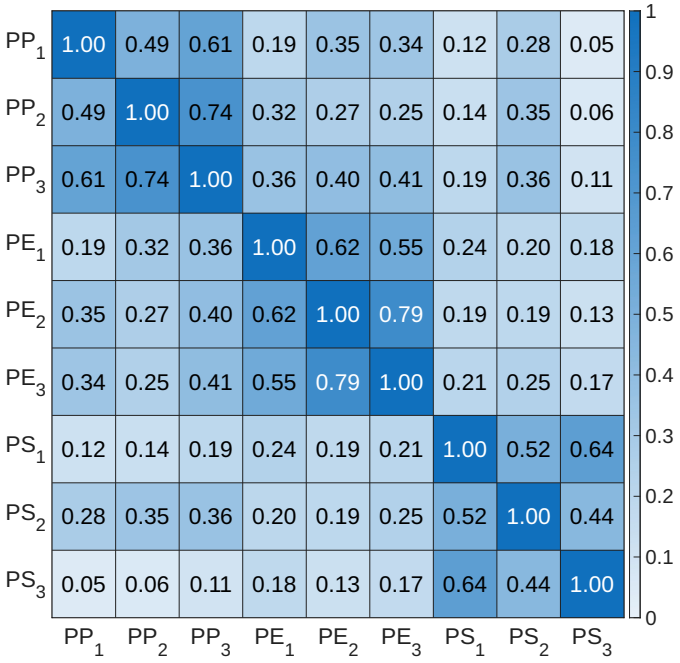

Fig. 4. CWTGM Scores. Higher value means a better match.

V. Conclusions

In this work, we set out to apply the CWT to the domain of hyperspectral remote sensing for marine plastic litter. A qualitative analysis of the resulting scalograms indicated that even when different polymer types share the same strong absorption regions, the CWT allows us to reveal the underlying signal structure and identify key features that enable material differentiation. Our findings suggest that a resolution of $10\,\mathrm{nm}$ is desirable to distinguish between PP, PE and PS.

To leverage these insights, we introduced CWTGM, a new technique that directly operates on the domain of CWT scalograms. Our technique was able to successfully group spectra of the same material type. Threshold-based applications of CWTGM appear promising, but more work is needed to verify that in-group and out-group match scores do not overlap when testing multiple materials, and to increase the margin between them to ensure reliable discrimination. There is a potential risk that in-group and out-group match scores may overlap in future analyses, in which case applying a threshold per material type could serve as a viable alternative.

While significant room for improvement remains, we believe that our results highlight the potential of CWT-based methods for enhancing the detection and classification of plastic materials in hyperspectral data. In addition, these approaches may not only inform the design and specification of future hyperspectral sensors, but also support more targeted band selection strategies - each with their own specifically tailored spectral resolution - by identifying scalogram regions where discriminant features reside. We believe these directions could lead to more robust, frequency-aware techniques for plastic litter detection in marine environments.

As future work, we propose that our methodology can be improved by extending the analysis to include additional polymer types and other forms of marine debris, with particular focus on underutilized datasets such as (K), explore the use of alternative wavelet parameters, and further expand on the CWTGM technique or similarly inspired approaches.

Data and Code Availability Notice

The original datasets (K) and (L) are available online at [19] and [20], respectively. Please note that we made use of the updated 2024 release of the (L) dataset. All of the code used to produce this work has been made available at [21] under the MIT license. Both datasets are also mirrored in the code repository, under their respective licenses.

Dataset Author Correspondence and Clarifications on Referenced Data

We contacted Dr. Els Knaeps regarding a labeling inconsistency in Table 2 of their paper and obtained confirmation that the label “PET Cups” was meant to be “LD-PE Cups”.

We also reached out to Dr. Giulia Leone, who confirmed an inconsistency in the metadata of IDs 201–205, where column “EMODnet micro-litter polymer type” mislabeled the sample as being “Polystyrene (PS)” when it should have been “Polypropylene (PP)”.

We appreciate the correspondence with both authors and thank them for their helpful clarifications.

References

[1] OECD, *Global Plastics Outlook: Economic Drivers, Environmental Impacts and Policy Options*. Paris: OECD Publishing, 2022. DOI: 10.1787/de747aef-en.

[2] OECD, *Policy Scenarios for Eliminating Plastic Pollution by 2040*. Paris: OECD Publishing, 2024. DOI: 10.1787/76400890-en.

[3] M. L. Haarr, J. Falk-Andersson, and J. Fabres, “Global marine litter research 2015–2020: Geographical and methodological trends,” *Science of The Total Environment*, vol. 820, p. 153 162, 2022, ISSN: 0048-9697. DOI: 10.1016/j.scitotenv.2022.153162.

[4] V. Martínez-Vicente *et al.*, “Measuring marine plastic debris from space: Initial assessment of observation requirements,” *Remote Sensing*, vol. 11, no. 20, 2019. DOI: 10.3390/rs11202443.

[5] M. Waqas, M. S. Wong, A. Stocchino, S. Abbas, S. Hafeez, and R. Zhu, “Marine plastic pollution detection and identification by using remote sensing-meta analysis,” *Marine Pollution Bulletin*, vol. 197, p. 115 746, 2023, ISSN: 0025-326X. DOI: 10.1016/j.marpolbul.2023.115746.

[6] N. Gnann, B. Baschek, and T. A. Ternes, “Close-range remote sensing-based detection and identification of macroplastics on water assisted by artificial intelligence: A review,” *Water Research*, vol. 222, p. 118 902, 2022, ISSN: 0043-1354. DOI: 10.1016/j.watres.2022.118902.

[7] S. P. Garaba and H. M. Dierssen, "An airborne remote sensing case study of synthetic hydrocarbon detection using short wave infrared absorption features identified from marine-harvested macro- and microplastics," *Remote Sensing of Environment*, vol. 205, pp. 224–235, 2018, ISSN: 0034-4257. DOI: 10.1016/j.rse.2017.11.023.

[8] M. Moshtaghi, E. Knaeps, S. Sterckx, S. Garaba, and D. Meire, "Spectral reflectance of marine macroplastics in the VNIR and SWIR measured in a controlled environment," *Scientific Reports*, vol. 11, no. 1, p. 5436, Mar. 2021, ISSN: 2045-2322. DOI: 10.1038/s41598-021-84867-6.

[9] M. Balsi, M. Moroni, V. Chiarabini, and G. Tanda, "High-resolution aerial detection of marine plastic litter by hyperspectral sensing," *Remote Sensing*, vol. 13, no. 8, 2021. DOI: 10.3390/rs13081557.

[10] P. Tasseron, T. van Emmerik, J. Peller, L. Schreyers, and L. Biermann, "Advancing floating macroplastic detection from space using experimental hyperspectral imagery," *Remote Sensing*, vol. 13, no. 12, 2021. DOI: 10.3390/rs13122335.

[11] K. Kikaki, I. Kakogeorgiou, P. Mikeli, D. E. Raitsos, and K. Karantzalos, "MARIDA: A benchmark for marine debris detection from Sentinel-2 remote sensing data," *PLoS One*, 2022. DOI: 10.1371/journal.pone.0262247.

[12] S. Mallat, *A Wavelet Tour of Signal Processing: The Sparse Way*, 3rd ed. Academic Press, 2008, ISBN: 9780123743701.

[13] E. Knaeps *et al.*, "Hyperspectral-reflectance dataset of dry, wet and submerged marine litter," *Earth System Science Data*, vol. 13, no. 2, pp. 713–730, 2021. DOI: 10.5194/essd-13-713-2021.

[14] G. Leone, A. I. Catarino, L. De Keukelaere, M. Bossaer, E. Knaeps, and G. Everaert, "Hyperspectral reflectance dataset of pristine, weathered, and biofouled plastics," *Earth System Science Data*, vol. 15, no. 2, pp. 745–752, 2023. DOI: 10.5194/essd-15-745-2023.

[15] G. Zhou *et al.*, "How many microplastics do we ingest when using disposable drink cups?" *Journal of Hazardous Materials*, vol. 441, p. 129 982, 2023, ISSN: 0304-3894. DOI: 10.1016/j.jhazmat.2022.129982.

[16] F. Du, H. Cai, Q. Zhang, Q. Chen, and H. Shi, "Microplastics in take-out food containers," *Journal of Hazardous Materials*, vol. 399, p. 122 969, 2020, ISSN: 0304-3894. DOI: 10.1016/j.jhazmat.2020.122969.

[17] S. Olhede and A. Walden, "Generalized morse wavelets," *IEEE Transactions on Signal Processing*, vol. 50, no. 11, pp. 2661–2670, 2002. DOI: 10.1109/TSP.2002.804066.

[18] J. M. Lilly and S. C. Olhede, "Generalized morse wavelets as a superfamily of analytic wavelets," *IEEE Transactions on Signal Processing*, vol. 60, no. 11, pp. 6036–6041, 2012. DOI: 10.1109/TSP.2012.2210890.

[19] *Dataset: Hyperspectral reflectance of marine plastics in the vis to swir*. [Online]. Available: https://doi.org/10.4121/12896312.v2.

[20] *Dataset: Hyperspectral reflectance dataset for dry, wet and submerged plastics in clear and turbid water*. [Online]. Available: https://doi.org/10.14284/530.

[21] *Code repository*. [Online]. Available: https://github.com/JMaravalhasSilva/cwt-spectral-analysis-marine-plastics.